Chiral extrapolation beyond the power-counting regime

J. M. M. Hall,[1] F. X. Lee,[2] D. B. Leinweber,[1] K. F. Liu,[3] N. Mathur,[4] R. D. Young,[1,5] and J. B. Zhang[6]

[1]*Special Research Centre for the Subatomic Structure of Matter (CSSM), School of Chemistry and Physics, University of Adelaide 5005, Australia*

[2]*Physics Department, The George Washington University, Washington, D.C. 20052, USA*

[3]*Department of Physics and Astronomy, University of Kentucky, Lexington, Kentucky 40506, USA*

[4]*Department of Theoretical Physics, Tata Institute of Fundamental Research, Mumbai, India*

[5]*ARC Centre of Excellence for Particle Physics at the Terascale, School of Chemistry and Physics, University of Adelaide 5005, Australia*

[6]*ZIMP and Department of Physics, Zhejiang University, Hangzhou, 310027, P. R. China*

(Received 26 January 2011; revised manuscript received 21 August 2011; published 9 December 2011)

Chiral effective field theory can provide valuable insight into the chiral physics of hadrons when used in conjunction with nonperturbative schemes such as lattice quantum chromodynamics (QCD). In this discourse, the attention is focused on extrapolating the mass of the ρ meson to the physical pion mass in quenched QCD. With the absence of a known experimental value, this serves to demonstrate the ability of the extrapolation scheme to make predictions without prior bias. By using extended effective field theory developed previously, an extrapolation is performed using quenched lattice QCD data that extends outside the chiral power-counting regime. The method involves an analysis of the renormalization flow curves of the low-energy coefficients in a finite-range regularized effective field theory. The analysis identifies an optimal regularization scale, which is embedded in the lattice QCD data themselves. This optimal scale is the value of the regularization scale at which the renormalization of the low-energy coefficients is approximately independent of the range of quark masses considered. By using recent precision, quenched lattice results, the extrapolation is tested directly by truncating the analysis to a set of points above 380 MeV, while temporarily disregarding the simulation results closer to the chiral regime. This tests the ability of the method to make predictions of the simulation results, without phenomenologically motivated bias. The result is a successful extrapolation to the chiral regime.

DOI: 10.1103/PhysRevD.84.114011 PACS numbers: 12.39.Fe, 11.10.Jj, 12.38.Aw, 12.38.Gc

I. INTRODUCTION

In lattice quantum chromodynamics (QCD), the calculation of observables with light dynamical quarks is computationally intensive, and only in recent times have there been successful attempts to perform calculations of any observable at the physical point ($m_\pi = 140$ MeV) [1–3]. Usually, some extrapolation scheme is needed if one is to compare theoretical calculations with the corresponding physical observables. Utilizing lattice QCD results spread over a larger range of quark masses naturally enables greater statistical precision in the extrapolation.

Quenched QCD (QQCD) was introduced as a way to ameliorate the computational difficulty of simulating dynamical fermions on the lattice. Quenched simulations typically have been superseded by the wide availability of dynamical configurations. Nevertheless, they can still be used as an efficient testing ground. This is particularly true of the chiral extrapolation problem, where the experimentally known values may introduce a prejudice on a chosen form. In QQCD, the physical target point does not exist, and an extrapolation of moderate-mass points to the chiral regime provides an unbiased test of the procedure.

In order to discuss the chiral behavior of the ρ meson in QQCD, one first constructs an effective field theory describing the relevant low-energy degrees of freedom. The mass of the ρ meson is described by a chiral expansion in the quark mass (m_q), which includes analytic terms that are polynomial in m_q, and nonanalytic terms arising from chiral loop integrals. These loop integrals are commonly divergent, and thus it is necessary to introduce a regularization procedure. Finite-range regularization (FRR) is selected as a regularization scheme, which introduces a momentum cutoff scale Λ into the loop integrals. The properties of FRR allow it to be used with data extending outside the power-counting regime (PCR), at the expense of complete scheme independence. As has been demonstrated, an optimal choice of regularization scale, Λ_{scale}, can be extracted from the lattice simulation results [4]. A systematic uncertainty in Λ_{scale} can also be estimated, which provides a range of suitable values for the scale obtained from the data [5]. Thus the scheme dependence in using data extending outside the PCR can be quantified in an unbiased fashion.

II. EXTENDED EFFECTIVE FIELD THEORY

In chiral effective field theory (χEFT), the diagrammatic formulation can be used to identify the major contributions to the ρ meson mass in QQCD [6,7]. The leading-order diagrams are the double and single η' hairpin diagrams as shown in Figs. 1 and 2, respectively. The constant

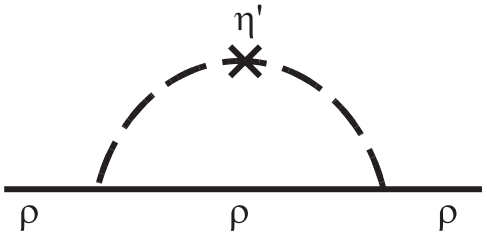

FIG. 1. Double hairpin η' diagram.

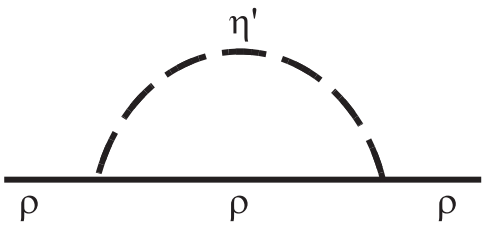

FIG. 2. Single hairpin η' diagram.

coefficients of these loop integrals are endowed with an uncertainty to encompass the possible effects of smaller contributions to order $\mathcal{O}(m_\pi^4)$.

Interactions with the flavor singlet η' are the most important contributions to the ρ meson mass in QQCD. This is an artifact of the quenched approximation, where the η' also behaves as a pseudo-Goldstone boson, having a ''mass'' that is degenerate with the pion. The dressing of the ρ meson by the η' field is illustrated in Figs. 3–5. Since the hairpin vertex must be a flavor singlet, the mesons that can contribute are the η' meson, and the ω meson. The contributions from the ω meson are insignificant due to Okubo-Zweig-Iizuka suppression and the small ρ-ω mass splitting. However, in QQCD, the η' loop behaves much as a pion loop, yet with a slightly modified propagator.

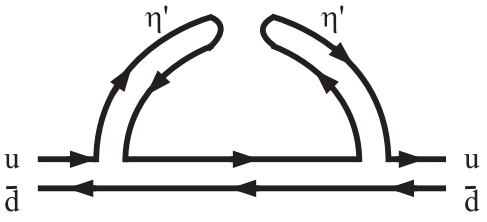

FIG. 3. Double hairpin quark flow diagram.

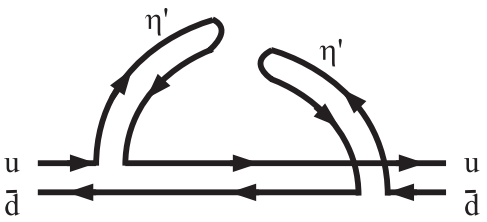

FIG. 4. Alternative double hairpin quark flow diagram.

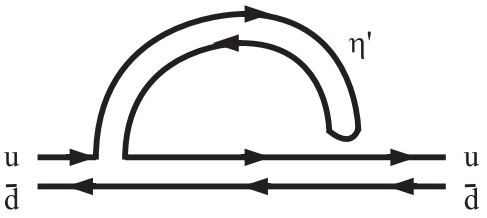

FIG. 5. Single hairpin quark flow diagram.

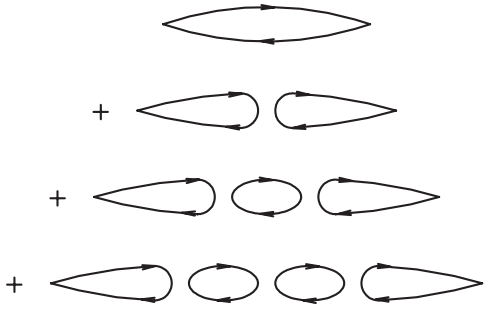

FIG. 6. Diagrammatic representation of η' propagator terms.

In full QCD however, the η' does not play any role in the low-energy dynamics. The physical η' acquires a finite mass—which survives in the chiral limit—by resumming the chain of vacuum insertions as depicted in Fig. 6. As a ''heavy'' degree of freedom, the η' can then be integrated out of the of the effective field theory.

A. Loop integrals and definitions

Using the Gell–Mann-Oakes-Renner Relation connecting quark and pion masses (assuming negligible anomalous scaling), $m_q \propto m_\pi^2$ [8], the ρ meson mass extrapolation formula in QQCD can be expressed in a form that contains an analytic polynomial in m_π^2 plus the chiral loop integrals (Σ^Q)

$$m_{\rho,Q}^2 = a_0 + a_2 m_\pi^2 + a_4 m_\pi^4 + \Sigma^Q_{\eta'\eta'}(m_\pi^2, \Lambda) + \Sigma^Q_{\eta'}(m_\pi^2, \Lambda) + \mathcal{O}(m_\pi^5). \quad (1)$$

The coefficients a_i are the ''residual series'' coefficients, which correspond to direct quark-mass insertions in the underlying Lagrangian of chiral perturbation theory. However, the nonanalytic behavior of the expansion arises from the chiral loop integrals. Upon renormalization of the divergent loop integrals, these will correspond with low-energy constants of the quenched χEFT. The extraction of these parameters from lattice QCD results will now be demonstrated.

By convention, the nonanalytic terms from the double and single hairpin integrals are $\chi_1 m_\pi$ and $\chi_3 m_\pi^3$, respectively. The coefficients χ_1 and χ_3 of the leading-order nonanalytic terms are scheme-independent constants that can be estimated from phenomenology. The low-order

expansion of the loop contributions takes the following form:

$$\Sigma^{Q}_{\eta'\eta'} = b_0^{\eta'\eta'} + \chi_1 m_\pi + b_2^{\eta'\eta'} m_\pi^2 + \chi_3^{\eta'\eta'} m_\pi^3 + b_4^{\eta'\eta'} m_\pi^4 + \mathcal{O}(m_\pi^6), \quad (2)$$

$$\Sigma^{Q}_{\eta'} = b_0^{\eta'} + b_2^{\eta'} m_\pi^2 + \chi_3^{\eta'} m_\pi^3 + b_4^{\eta'} m_\pi^4 + \mathcal{O}(m_\pi^6). \quad (3)$$

The coefficient χ_3 is obtained by adding the contributions from both integrals, $\chi_3 = \chi_3^{\eta'\eta'} + \chi_3^{\eta'}$. Each integral has a solution in the form of a polynomial expansion analytic in m_π^2 plus nonanalytic terms, of which the leading-order term is of greatest interest. The coefficients b_i are scale-dependent and therefore scheme-dependent. In order to achieve an extrapolation based on an optimal FRR scale, first the scale dependence of the low-energy expansion must be removed through renormalization. The renormalization program of FRR combines the scheme-dependent b_i coefficients from the chiral loops with the scheme-dependent a_i coefficients from the residual series at each chiral order i. The result is a scheme-independent coefficient c_i

$$c_0 = a_0 + b_0^{\eta'\eta'} + b_0^{\eta'}, \quad (4)$$

$$c_2 = a_2 + b_2^{\eta'\eta'} + b_2^{\eta'}, \quad (5)$$

$$c_4 = a_4 + b_4^{\eta'\eta'} + b_4^{\eta'}, \text{ etc.} \quad (6)$$

That is, the underlying a_i coefficients undergo a renormalization from the chiral loop integrals. The renormalized coefficients c_i are an important part of the extrapolation technique. A stable and robust determination of these parameters forms the core of determining an optimal scale Λ^{scale}.

The loop integrals can be expressed in a convenient form by taking the nonrelativistic limit and performing the pole integration for k_0. Renormalization is achieved by subtracting the relevant terms in the Taylor expansion of the loop integrals and absorbing them into the corresponding low-energy coefficients, c_i

$$\tilde{\Sigma}^{Q}_{\eta'\eta'}(m_\pi^2;\Lambda) = \frac{-\chi_{\eta'\eta'}}{3\pi^2}\int d^3k \frac{(M_0^2k^2 + \frac{5}{2}A_0k^4)u^2(k;\Lambda)}{(k^2+m_\pi^2)^2} - b_0^{\eta'\eta'} - b_2^{\eta'\eta'} m_\pi^2 - b_4^{\eta'\eta'} m_\pi^4, \quad (7)$$

$$\tilde{\Sigma}^{Q}_{\eta'}(m_\pi^2;\Lambda) = \frac{\chi_{\eta'}}{2\pi^2}\int d^3k \frac{k^2u^2(k;\Lambda)}{k^2+m_\pi^2} - b_0^{\eta'} - b_2^{\eta'} m_\pi^2 - b_4^{\eta'} m_\pi^4. \quad (8)$$

The tilde () denotes that the integrals are written out in renormalized form to chiral order $\mathcal{O}(m_\pi^4)$. The coefficients $\chi_{\eta'\eta'}$ and $\chi_{\eta'}$ are related to the coefficients of the leading-order nonanalytic terms by

$$\chi_1 = M_0^2 \chi_{\eta'\eta'}, \quad (9)$$

$$\chi_3 = \chi_3^{\eta'\eta'} + \chi_3^{\eta'} = A_0\chi_{\eta'\eta'} + \chi_{\eta'}. \quad (10)$$

These couplings are discussed in detail below. The function $u(k;\Lambda)$ is a finite-range regulator with cutoff scale Λ, which must be normalized to 1 at $k^2 = 0$, and must approach 0 sufficiently fast to ensure convergence of the loop. Different functional forms of $u(k;\Lambda)$ are equivalent within the PCR [9,10]. Different choices of $u(k;\Lambda)$ for this investigation are discussed in Sec. II B.

With the loop integrals specified, Eq. (1) can be rewritten in terms of the renormalized coefficients c_i

$$m_{\rho,Q}^2 = c_0 + c_2 m_\pi^2 + c_4 m_\pi^4 + \tilde{\Sigma}^{Q}_{\eta'\eta'}(m_\pi^2;\Lambda) + \tilde{\Sigma}^{Q}_{\eta'}(m_\pi^2;\Lambda) + \mathcal{O}(m_\pi^5) \quad (11)$$

$$\approx c_0 + \chi_1 m_\pi + c_2 m_\pi^2 + \chi_3 m_\pi^3 + c_4 m_\pi^4 + \mathcal{O}(m_\pi^5). \quad (12)$$

Equation (11) will be used as the extrapolation formula for $m_{\rho,Q}$ at infinite lattice volume. The fit coefficients are c_0, c_2 and c_4, and $m_{\rho,Q}$ is obtained by taking the square root of Eqs. (11) and (12). It is important to note that the formula in Eq. (12) is equivalent to Eq. (11) only as Λ is taken to infinity.

Since lattice simulations are necessarily carried out on a discrete spacetime, any extrapolations performed should take into account finite-volume effects. The low-energy effective field theory is ideally suited for characterizing the leading infrared effects associated with the finite volume. In order to achieve this, each of the three-dimensional integrals can be transformed to its form on the lattice using a finite sum of discretized momenta, following Armour *et al.* [7], for instance,

$$\int \mathrm{d}^3k \to \frac{(2\pi)^3}{L_xL_yL_z}\sum_{k_x,k_y,k_z}. \quad (13)$$

Each momentum component is quantized in units of $2\pi/L$, that is $k_i = n_i 2\pi/L$ for integers n_i. Finite-volume corrections δ^{FVC} can be written simply as the difference between the finite sum and the corresponding integral. It is known that the finite-volume corrections saturate to a fixed result for large values of the regularization scale [4]. Following the example set by this article, the value $\Lambda' = 2.0$ GeV is chosen to evaluate all finite-volume corrections independent of the FRR cutoff scale Λ in Eqs. (7) and (8). The finite-volume version of Eq. (11) can thus be expressed

$$m_{\rho,Q}^2 = c_0 + c_2 m_\pi^2 + c_4 m_\pi^4 + (\tilde{\Sigma}^{Q}_{\eta'\eta'}(m_\pi^2;\Lambda) + \delta^{\text{FVC}}_{\eta'\eta'}(m_\pi^2;\Lambda')) + (\tilde{\Sigma}^{Q}_{\eta'}(m_\pi^2;\Lambda) + \delta^{\text{FVC}}_{\eta'}(m_\pi^2;\Lambda')) + \mathcal{O}(m_\pi^5). \quad (14)$$

The convention used for defining the values of χ_1, χ_3, and the various coupling constants that occur in each, follows Booth [11]. For the possible different values that

coupling constants can take, definitions by Chow and Rey [6], Armour *et al.* [7] and Sharpe [12] are used. The types of vertices available are shown in Fig. 7, where g_2 and g_4 occur explicitly in the two diagrams considered here. Booth suggests naturalness for $g_2 \sim 1$, and that $g_4 \sim 1/N_c$. These quenched coupling constants can be connected with the experimental value of $g_{\omega\rho\pi}$ as per Lublinsky [13] by the relation

$$g_2 = \frac{1}{2} g_{\omega\rho\pi} f_\pi, \tag{15}$$

where $g_{\omega\rho\pi} = 14 \pm 2\ \mathrm{GeV}^{-1}$ and the pion decay constant takes the value $f_\pi = 0.0924$ GeV. Thus g_2 is chosen to be 0.65 ± 0.09 GeV and g_4 is chosen to be approximately $g_2/3$. The coupling between the separate legs of the double hairpin diagram are approximated by the massive constant $M_0^2 \propto m_{\eta'}^2$. The next-order correction to M_0 in momentum k defines the coupling to be $-M_0^2 + A_0 k^2$. These constants can be connected to the full QCD η' meson mass $m_{\eta'}$ by considering the geometric series of terms as previously illustrated in Fig. 6. For the value of M_0, Booth suggest $M_0 \approx 400$ MeV by comparing the estimate from a hairpin insertion to the result from the Witten-Veneziano formula [11]. In a paper by Duncan *et al.* a value of $M_0 \approx 900$ MeV is obtained if the coupling constant A_0 is natural. Furthermore, an analysis of the topological susceptibility leads to an estimate $M_0 = 1.1 \pm 0.2$ GeV [14]. In this analysis, an average value $M_0 = (400 + 900 + 1100)/3 = 800$ MeV is sensible as a first approximation. As a further check, consider the formula from Ref. [14], using our normalization for the pion decay constant ($f_\pi^2 = 2f_{\pi,\mathrm{Duncan}}^2$)

$$\delta = \frac{A_0 M_0^2}{48\pi^2 f_\pi^2}. \tag{16}$$

This formula relates the couplings A_0 and M_0^2 to the anomalous scaling parameter of the pion mass in quenched QCD, defined by

$$m_\pi^2 \approx m_q^{1/1+\delta}. \tag{17}$$

The parameter δ is found to be small (and the Gell–Mann-Oakes-Renner Relation a good approximation), with a maximum value estimated by Duncan to be $\delta_{\max} = 0.03$ [14]. Booth comments that the parameter A_0 is small, and vanishes in the limit $N_c \to \infty$. Nevertheless, Sharpe uses a finite value $A_0 \sim 0.2$ [12]. By using these finite values for δ and A_0, Eq. (16) leads to a value of $M_0^2 \approx 0.6\ \mathrm{GeV}^2$. As a result, M_0^2 is taken to be $0.6 \pm 0.2\ \mathrm{GeV}^2$ and A_0 is taken to be 0 ± 0.2.

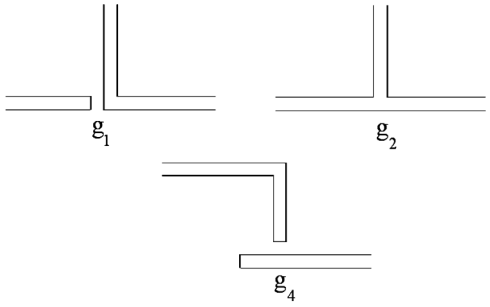

FIG. 7. Coupling types following convention introduced by Booth [11].

The coefficients $\chi_{\eta'\eta'}$ and $\chi_{\eta'}$ can be specified in terms of the relevant coupling constants

$$\chi_{\eta'\eta'} = -2\mathring{m}_\rho \frac{g_2^2}{4\pi f_\pi^2}, \qquad \chi_{\eta'} = -2\mathring{m}_\rho \frac{g_2 g_4}{6\pi f_\pi^2}, \tag{18}$$

where the couplings are defined relative to $\mathring{m}_\rho$ representing the ρ meson mass in the chiral limit, which is taken to be 770 MeV.

B. Finite-range regularization

In FRR, regulator functions $u(k;\Lambda)$ with characteristic scale Λ are inserted into the loop integrals to control the ultraviolet divergences that occur in the loop integrals encountered. For some choices of regulator, extra regulator-dependent nonanalytic terms arise in the chiral expansion of Eq. (12). Since the correct nonanalytic terms of the chiral expansion are regularization scale-independent terms, the extra nonanalytic terms within working chiral order must be removed. All scale dependence should be absorbed into the analytic fit parameters a_i. For example, if a dipole regulator is chosen, the extra terms $b_3^{(1)} m_\pi^3$, $(b_5^{(1)} + b_5^{(3)}) m_\pi^5$ and higher-order terms occurring at odd powers of m_π feature in Eq. (12). One can avoid this by choosing a regulator that does not generate these extra terms, up to working-order $\mathcal{O}(m_\pi^4)$. Since the step function $u^2(k;\Lambda) = \theta(\Lambda - k)$ introduces inconvenient finite-volume artifacts, a "triple-dipole" form factor will be chosen, defined by

$$u(k;\Lambda) = \left(1 + \left[\frac{k^2}{\Lambda^2}\right]^3\right)^{-2}. \tag{19}$$

III. LATTICE SIMULATION DETAILS

The calculation is performed on a $20^3 \times 32$ lattice with 197 gauge configurations generated with the Iwasaki gauge action [15] at $\beta = 2.264$, and the quark propagators are calculated with overlap fermions and a wall source technique. The lattice spacing is 0.153 fm, as determined from the Sommer scale parameter.

The massive overlap Dirac operator is defined [16] in the following way so that at tree level there is no mass or wave function renormalization [17]:

$$D(m) = \rho + \frac{m}{2} + \left(\rho - \frac{m}{2}\right)\gamma_5 \epsilon(H), \tag{20}$$

where $\epsilon(H)$ is the matrix sign function of an Hermitian operator H. $\epsilon(H) \equiv H_W/|H_W| = H_W/(H_W^\dagger H_W)^{1/2}$ is

chosen, where $H_W(x, y) = \gamma_5 D_W(x, y)$. Here D_W is the usual Wilson-Dirac operator on the lattice, except with a negative mass parameter $-\rho = 1/2\kappa - 4$ in which $\kappa_c < \kappa < 0.25$. Taking $\kappa = 0.19$ in the calculation corresponds to $\rho = 1.368$ [18,19].

In Fig. 8 the simulation results for the vector meson mass are shown for a range of quark masses.

The data displayed in Fig. 8 are split into two parts. All the data left of the solid vertical line are unused for extrapolation and kept in reserve. Indeed, the authors performing the extrapolation were blind to these data. This is so that the extrapolation can be checked against these known data points once the extrapolation is established. In other words, the results of the chiral extrapolation are genuine *predictions* of the hidden lattice results. Only the data points to the right of the solid vertical line are used for extrapolation. The full set of data is also listed in Table I, which also includes the bare quark-mass values. In addition, effective mass plots corresponding to four lighter pion masses are included, in Figs. 9–12.

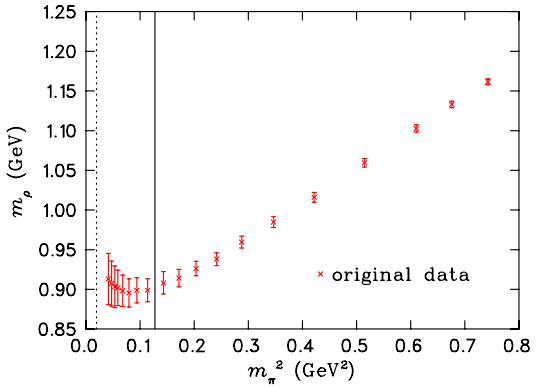

FIG. 8 (color online). Quenched lattice QCD data for the ρ meson mass. The dashed vertical line indicates the physical pion mass and the solid vertical line shows how the data set is split into two parts. The lower-mass portion of the data was not known at the time of extrapolation.

TABLE I. Quenched lattice QCD data for the ρ meson mass m_ρ at various pion mass squared values m_π^2. The statistical uncertainty of the m_π^2 is negligible. The values of the bare quark mass m_q are also included for comparison. The lattice size is $20^3 \times 32$, with a lattice spacing of 0.153 fm. Entries below the line (underneath $m_\pi^2 = 0.143$ GeV^2) remained hidden until the extrapolation was determined.

m_q (GeV)	m_π^2(GeV^2)	m_ρ (GeV)	$m_\pi L$
1.032	3.150	2.001(1)	27.53
0.774	2.187	1.700(2)	22.94
0.645	1.742	1.548(2)	20.47
0.516	1.329	1.399(2)	17.88
0.477	1.212	1.354(2)	17.08
0.426	1.062	1.294(2)	15.98
0.356	0.867	1.214(3)	14.44
0.309	0.743	1.162(4)	13.37
0.284	0.676	1.133(4)	12.75
0.258	0.610	1.103(5)	12.12
0.219	0.515	1.060(5)	11.13
0.181	0.422	1.016(6)	10.07
0.148	0.347	0.985(7)	9.13
0.123	0.288	0.960(8)	8.32
0.102	0.241	0.938(8)	7.62
0.085	0.204	0.926(9)	7.00
0.071	0.172	0.914(11)	6.43
0.058	0.143	0.908(14)	5.87
0.045	0.114	0.899(15)	5.24
0.036	0.094	0.899(16)	4.75
0.030	0.080	0.896(18)	4.38
0.025	0.068	0.898(20)	4.04
0.021	0.059	0.902(22)	3.77
0.018	0.053	0.903(26)	3.58
0.015	0.047	0.907(28)	3.37
0.013	0.041	0.913(32)	3.15

To estimate finite-volume effects using overlap fermions, quenched lattices of volumes $16^3 \times 28$ and $12^3 \times 28$ with $a = 0.2$ fm are used. For a pion mass of 180 MeV, $m_{PS}L \approx 3$, and the finite-volume correction is approximately 2.7 MeV: about 1.5% of the pion mass [18]. The current $20^3 \times 32$ lattice with $a = 0.153$ fm is about the same physical size as that of a $16^3 \times 28$ lattice and a similar finite-volume correction is expected. To estimate the finite-volume correction of the lowest ρ meson mass at $m_\pi \approx 200$ MeV, the same percentage of error is used, and a shift of $\delta_L m_\rho \approx 13$ MeV to the ρ mass is calculated for the ρ meson mass of $m_\rho \approx 917$ MeV. This is about half of the statistical error of the lattice data. It should be noted that the data that will be used in chiral extrapolations are those with pion mass greater than 400 MeV, with $m_{PS}L > 6.2$. The predictions are extended to the region with pion mass less than 400 MeV and compared with the lattice data.

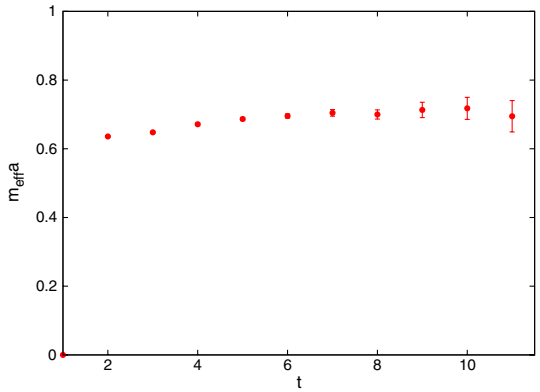

FIG. 9 (color online). Effective mass plot corresponding to the simulation at $m_\pi^2 = 0.143$ GeV^2. Only the wall source results are plotted. The point source results are not used in the analysis.

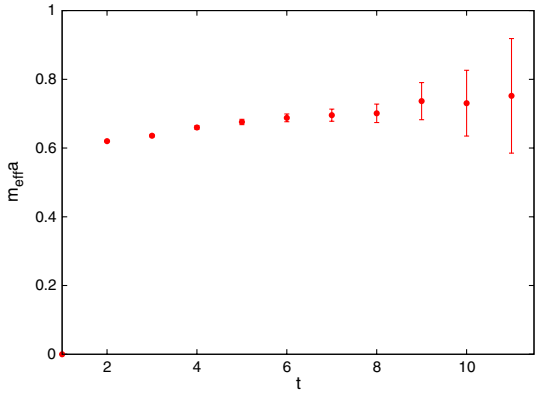

FIG. 10 (color online). Effective mass plot corresponding to the simulation at $m_\pi^2 = 0.080$ GeV^2. Only the wall source results are plotted. The point source results are not used in the analysis.

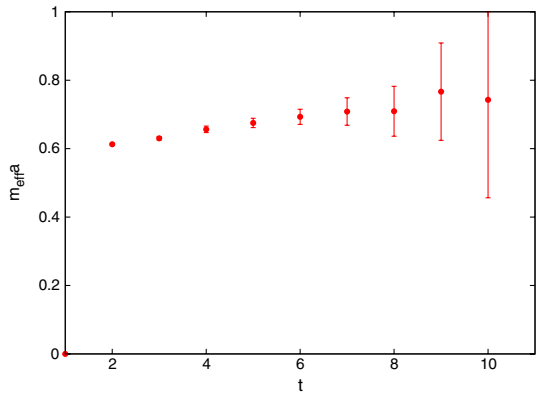

FIG. 12 (color online). Effective mass plot corresponding to the simulation at $m_\pi^2 = 0.041$ GeV^2. Only the wall source results are plotted. The point source results are not used in the analysis.

With regard to possible lattice artifacts, the lattice results analyzed are based on the overlap fermion on quenched gauge configurations at one lattice spacing. Even though the overlap fermion has relatively smaller $\mathcal{O}(a)$ errors, the $\mathcal{O}(a^2)$ correction toward the continuum limit has not been taken into account. With a spatial size of 3.06 fm, $m_\pi a \sim 3$ for the smallest pion mass at 200 MeV is somewhat smaller than $m_\pi a = 4$, beyond which the finite-volume effect has been considered to be small. For $m_\pi a \sim 3$, the previous study described in Ref. [18] estimates that the finite-volume correction is approximately 3% which is smaller than the statistical error of the pion mass.

The enhancement of zero modes effects in QQCD primarily affects the pseodoscalar and scalar mesons. Since all the zero modes appear in one chiral sector in each gauge configuration, the pseodoscalar and scalar mesons will have a leading $1/m^2$ singularity from the zero modes. These appear in both the quark and antiquark propagators in the meson correlator [17]. Nevertheless, the vector and axial vector mesons have only a $1/m$ singularity, which is a less dramatic effect. In either case, the quantity that determines the size of the zero mode effects is $m\Sigma V$ in the p-regime [20]. It has been demonstrated that when $m\Sigma V \gtrsim 5$, the zero mode effect is hardly detectable [18,21]. For all pion masses displayed in Fig. 12, $m\Sigma V > 7$. Therefore, there is no reason to suggest that there is a zero mode contribution to the ρ meson correlators being studied.

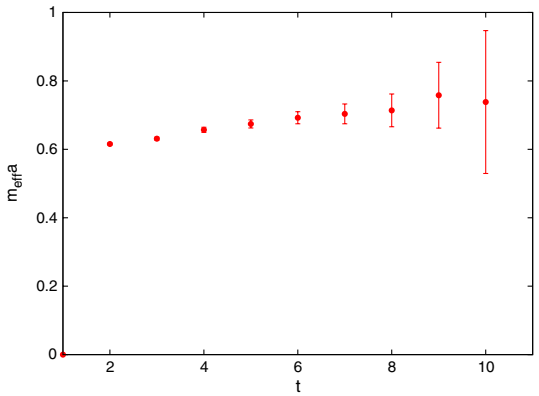

FIG. 11 (color online). Effective mass plot corresponding to the simulation at $m_\pi^2 = 0.053$ GeV^2. Only the wall source results are plotted. The point source results are not used in the analysis.

IV. EXTRAPOLATION RESULTS

A. Renormalization flow curves

In order to produce an extrapolation to each test value of m_π^2, a finite-range regularization scale Λ must be selected. As an example, one can choose a triple-dipole regulator at $\Lambda = 1.0$ GeV. By using Eq. (14), finite- and infinite-volume extrapolations are shown in Fig. 13. Note that the m_π^2 values selected for the finite-volume extrapolations exactly correspond to the "missing" low-energy data points set aside earlier. The physical point $m_\pi^2 = 0.0196$ GeV^2 is included as well.

Now the regularization scale dependence of low-energy coefficients c_0, c_2 and c_4 is investigated for various upper limits of the range of pion masses. The renormalization of these low-energy coefficients is considered for a series of Λ values. The aim is to obtain renormalization flow curves, each corresponding to a different value of maximum pion mass, $m_{\pi,\mathrm{max}}^2$. Thus the behavior of the renormalization of the low-energy coefficients can be examined as lattice data extend further outside the PCR. Figures 14–16 show the renormalization flow curves for each of c_0, c_2 and c_4. Note that each data point plotted has an associated error bar, but for the sake of clarity only a few points are selected to indicate the general size of the statistical error bars. Using the procedure described in Ref. [4], the optimal regularization scale is identified by the value of Λ that minimizes

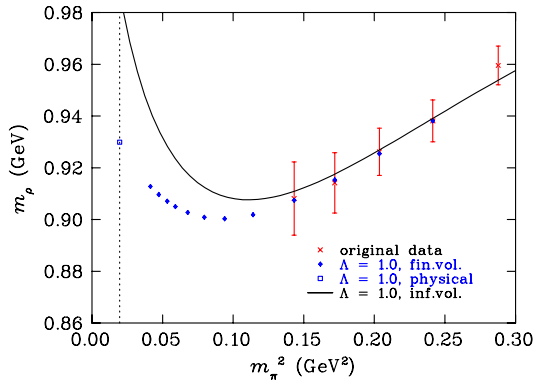

FIG. 13 (color online). A test extrapolation based on the four lightest original data points (excluding the low-energy set) as shown. Both the finite- and infinite-volume results are shown for a triple-dipole regulator at $\Lambda = 1.0$ GeV. The dashed vertical line indicates the physical pion mass.

the discrepancies among the renormalization flow curves. This indicates the value of regularization scale at which the renormalization of c_0, c_2 and c_4 is least sensitive to the truncation of the data. Physically, this value of Λ can be associated with an intrinsic scale related to the size of the source of the pion cloud.

By examining Figs. 14–16, increasing $m^2_{\pi,\max}$ leads to greater scheme dependence in the renormalization, since the data sample lies further from the PCR. Complete scheme independence would be indicated by a horizontal line at the physical point. Since the effective field theory is calculated to a finite chiral order, complete scheme independence across all possible values of Λ will not occur in practice. Note that an asymptotic value is usually observed in the renormalization flow as Λ becomes large, indicating that the higher-order terms of the chiral expansion are effectively zero. However, these asymptotic values of the low-energy coefficients are poor estimates of their correct values, as previously demonstrated in a pseudodata model [4]. Instead, the best estimates of the low-energy coefficients lie in the identification of the intersection point of

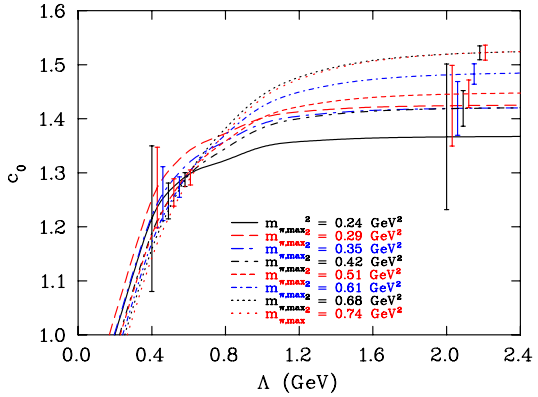

FIG. 14 (color online). behavior of c_0 vs Λ. A few points are selected to indicate the general size of the statistical error bars.

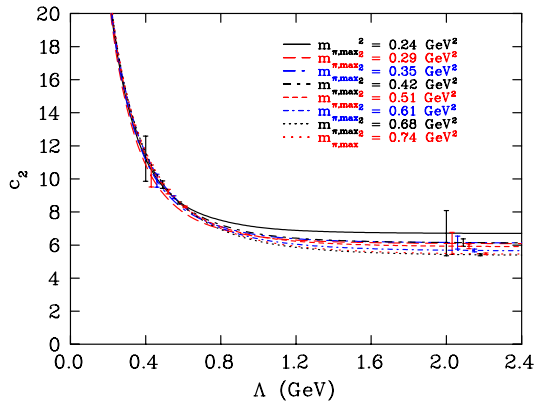

FIG. 15 (color online). behavior of c_2 vs Λ. A few points are selected to indicate the general size of the statistical error bars.

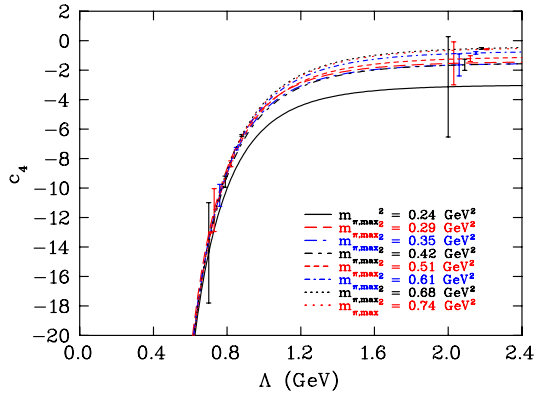

FIG. 16 (color online). behavior of c_4 vs Λ. A few points are selected to indicate the general size of the statistical error bars.

the renormalization flow of the low-energy coefficients. It is also of note that, for small values of Λ, FRR schemes break down. The regularization scale must be at least large enough to include the chiral physics being studied.

B. Optimal regularization scale

The optimal regularization scale Λ^{scale} can be obtained from the renormalization flow curves using a chi-square analysis described below. In addition, the analysis will allow the extraction of a range for Λ^{scale}. Knowing how the data are correlated, the systematic uncertainties from the coupling constants and Λ^{scale} will be combined to obtain an error bar for each extrapolation point. Of particular interest are the values of $m_{\rho,Q}$ at the values of m^2_π explored in the lattice simulations but excluded in the chiral extrapolation.

To obtain a measure of the uncertainty associated with an optimal regularization scale, a χ^2_{dof} function is constructed. This function should allow easy identification of the intersection points in the renormalization flow curves, and a range associated with this central regularization scale. The first step is to plot χ^2_{dof} against a series of Λ values. The relevant data are the extracted low-energy

coefficients with differing values of $m^2_{\pi,\max}$. A plot of $\chi^2_{\rm dof}$ is constructed separately for each renormalized coefficient c (with uncertainty δc)

$$\chi^2_{\rm dof} = \frac{1}{n-1}\sum_{i=1}^{n}\frac{(c(i;\Lambda)-c^T(\Lambda))^2}{(\delta c(i;\Lambda))^2}, \tag{21}$$

for i corresponding to fits with differing values of $m^2_{\pi,\max}$ ($n = 8$). The theoretical value c^T is given by the weighted mean

$$c^T(\Lambda) = \frac{\sum_{i=1}^{n} c(i;\Lambda)/(\delta c(i;\Lambda))^2}{\sum_{j=1}^{n} 1/(\delta c(j;\Lambda))^2}. \tag{22}$$

The $\chi^2_{\rm dof}$ plots using a triple-dipole regulator are shown in Figs. 17–19. The optimal regularization scale $\Lambda^{\rm scale}$ is taken to be the central value $\Lambda_{\rm central}$ of each plot. The upper and lower bounds obey the condition $\chi^2_{\rm dof} < \chi^2_{\rm dof,min} + 1/({\rm dof})$. The results for the optimal regularization scale and the upper and lower bounds are shown in Table II. It is remarkable that each low-energy coefficient leads to the same optimal value of Λ, i.e. $\Lambda_{\rm central} = 0.67$ GeV. By averaging the results among c_0, c_2, and c_4, the optimal regularization scale $\Lambda_{\rm scale}$ for the quenched ρ meson mass can be calculated for this data set: $\Lambda_{\rm scale} = 0.67^{+0.09}_{-0.08}$ GeV.

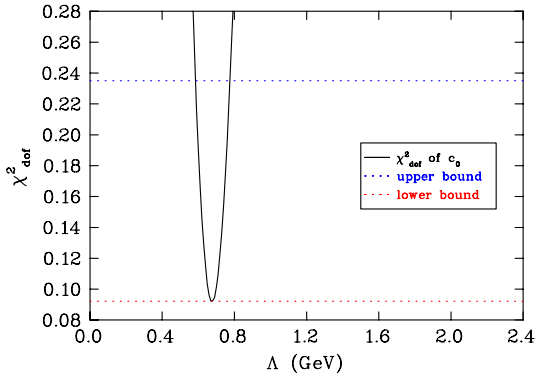

FIG. 17 (color online). $\chi^2_{\rm dof}$ for c_0 versus Λ, corresponding to the renormalization flow curves displayed in Fig. 14.

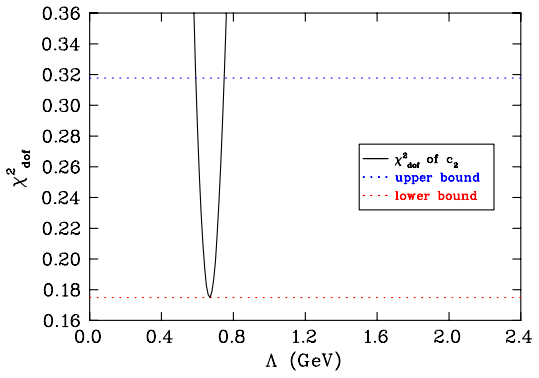

FIG. 18 (color online). $\chi^2_{\rm dof}$ for c_2 versus Λ, corresponding to the renormalization flow curves displayed in Fig. 15.

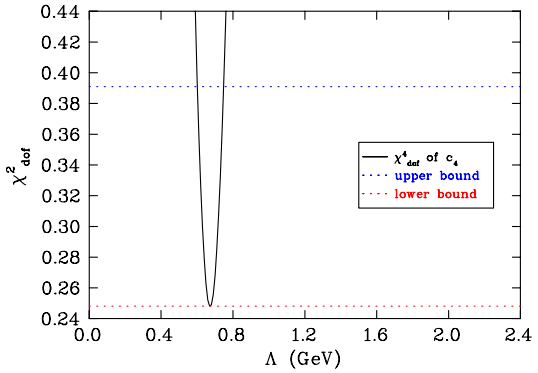

FIG. 19 (color online). $\chi^2_{\rm dof}$ for c_4 versus Λ, corresponding to the renormalization flow curves displayed in Fig. 16.

The result of the final extrapolation, using the estimate of the optimal regularization scale $\Lambda_{\rm scale} = 0.67^{+0.09}_{-0.08}$ GeV, and using the initial data set to predict the low-energy data points, is shown in Fig. 20. The extrapolation to the physical point obtained for this quenched data set is: $m^{\rm ext}_{\rho,Q}(m^2_{\pi,\rm phys}) = 0.925^{+0.053}_{-0.049}$ GeV, an uncertainty of less than 6%.

Note that each extrapolation point displays two error bars. The inner error bar corresponds to the systematic uncertainty in the parameters only, and the outer error bar corresponds to the systematic and statistical uncertainties of each point added in quadrature. Also, the infinite-volume extrapolation curve is displayed in order to illustrate the effect of finite-volume corrections to the loop integrals.

In Fig. 21, the extrapolation predictions are compared against the actual simulation results, which were not included in the fit. Note that both the extrapolations and the simulation results display the same nonanalytic curvature near the physical point. Figure 22 shows the data plotted with error bars correlated relative to the lightest data point in the original set, $m^2_\pi = 0.143$ GeV^2. This aids in clarifying the plot from Fig. 21 by removing much of the correlated statistical error in the lattice data, and allows us to be even more stringent in determining whether the extrapolation is successful. It is notable that the extrapolated results are consistent with the lattice data even after having removed the correlated statistical error. To highlight the importance of this application of an extended χEFT, a

TABLE II. Values of the central, upper and lower regularization scales, in GeV, obtained from the $\chi^2_{\rm dof}$ analysis of c_0, c_2 and c_4, displayed in Figs. 17–19.

scale (GeV)	c_0 (Fig. 17)	c_2 (Fig. 18)	c_4 (Fig. 19)
$\Lambda_{\rm central}$	0.67	0.67	0.67
$\Lambda_{\rm upper}$	0.78	0.75	0.75
$\Lambda_{\rm lower}$	0.58	0.59	0.60

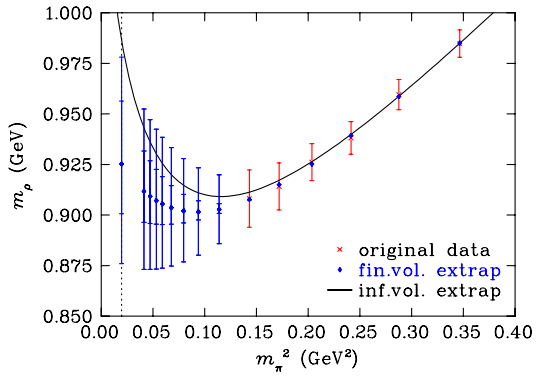

FIG. 20 (color online). Extrapolation at $\Lambda_{\text{scale}} = 0.67^{+0.09}_{-0.08}$ GeV based on Kentucky Group data, and using the optimal number of data points, corresponding to $\hat{m}^2_{\pi,\text{max}} = 0.35$ GeV^2. The inner error bar on the extrapolation points represents purely the systematic error from parameters. The outer error bar represents the systematic and statistical error estimates added in quadrature.

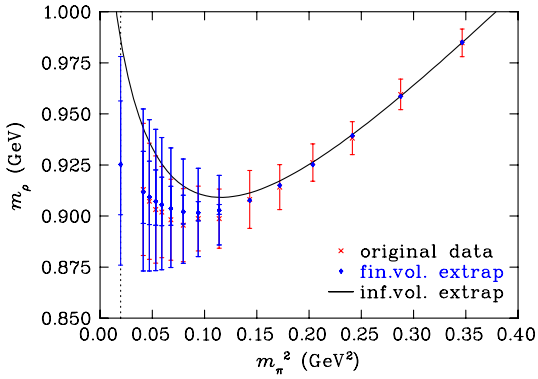

FIG. 21 (color online). Comparison of chiral extrapolation predictions (blue diamond) with Kentucky Group data (red cross). Extrapolation is performed at $\Lambda_{\text{scale}} = 0.67^{+0.09}_{-0.08}$ GeV, and using the optimal number of data points, corresponding to $\hat{m}^2_{\pi,\text{max}} = 0.35$ GeV^2. The inner error bar on the extrapolation points represents purely the systematic error from parameters. The outer error bar represents the systematic and statistical error estimates added in quadrature.

simple linear fit is included in Fig. 22. By ignoring low-energy chiral physics, the linear fit is statistically incorrect at the physical point. Note also that all of the missing original data points are consistent within the extrapolations' systematic uncertainties. After statistical correlations are subtracted, the extrapolated points correspond to an error bar almost half the size of that of the lattice data points. In order to match this precision at low energies, the time required in lattice simulations would increase by approximately 4 times.

In order to check if scheme independence is recovered using data within the PCR, the low-energy data that were initially excluded from analysis can now be treated in the same way. That is, renormalization flow curves can be

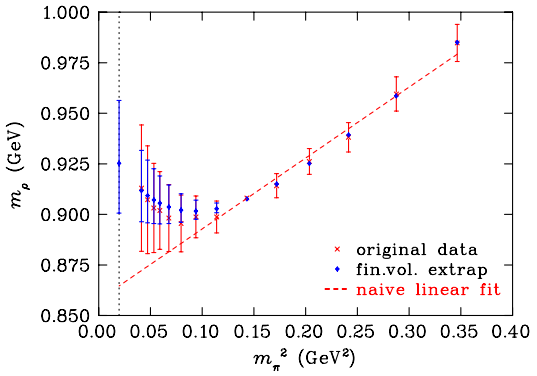

FIG. 22 (color online). Comparison of chiral extrapolation predictions (blue diamond) with Kentucky Group data (red cross), with errors correlated relative to the point at $m^2_\pi = 0.143$ GeV^2. This is done simply to clarify the plot in Fig. 21 by removing much of the correlated statistical error. Extrapolation is performed at $\Lambda_{\text{scale}} = 0.67^{+0.09}_{-0.08}$ GeV, and using the optimal number of data points, corresponding to $\hat{m}^2_{\pi,\text{max}} = 0.35$ GeV^2. The error bar on the extrapolation points represents the systematic error only. A simple linear fit, on the optimal pion mass region, is included for comparison.

constructed as a function of Λ for sequentially increasing $m^2_{\pi,\text{max}}$. The results are shown in Figs. 23–25. Clearly, the renormalization flow curves for each plot corresponding to c_0, c_2 and c_4 are flatter than those of the initial analysis, indicating a reduction in the regularization scale dependence due to the use of data closer to the PCR. One is not able to extract an optimal regularization scale from these plots, as shown in the behavior of χ^2_{dof}, displayed in Figs. 26–28. However, each χ^2_{dof} curve provides a lower bound for the regularization scale, where FRR breaks down [4], as discussed in Section IV A. These lower bounds are: $\Lambda^{c_0}_{\text{lower}} = 0.39$ GeV, $\Lambda^{c_2}_{\text{lower}} = 0.52$ GeV and $\Lambda^{c_4}_{\text{lower}} = 0.59$ GeV.

The statistical error bars of the low-energy coefficients corresponding to a small number of data points in

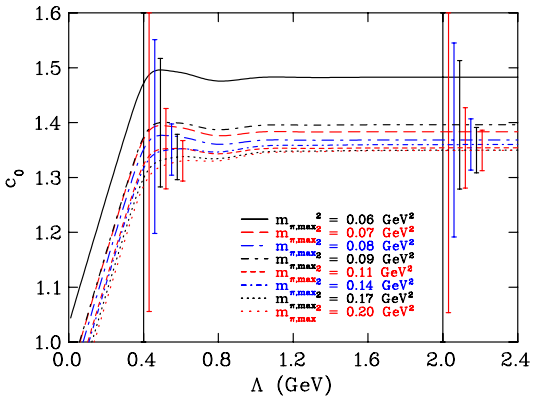

FIG. 23 (color online). behavior of c_0 vs Λ including the initially excluded low-energy data. A few points are selected to indicate the general size of the statistical error bars.

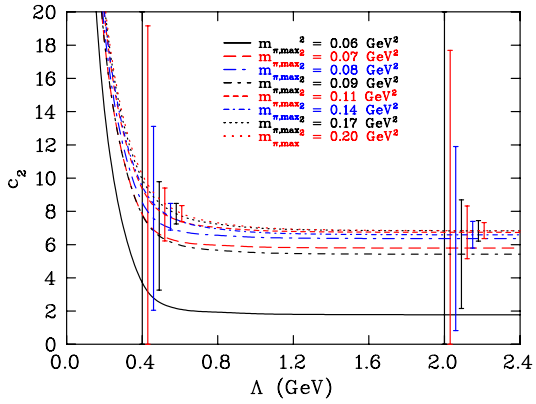

FIG. 24 (color online). behavior of c_2 vs Λ including the initially excluded low-energy data. A few points are selected to indicate the general size of the statistical error bars.

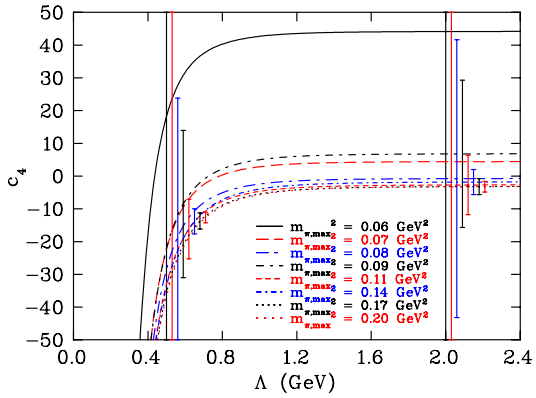

FIG. 25 (color online). behavior of c_4 vs Λ including the initially excluded low-energy data. A few points are selected to indicate the general size of the statistical error bars.

Figs. 23–25 is large, and a statistical difference among the curves does not appear until $m^2_{\pi,\mathrm{max}} \approx 0.11$ GeV^2. Thus the identification of an optimal regularization scale will be aided by incorporating data corresponding to even larger values of $m^2_{\pi,\mathrm{max}}$. By considering *all* of the available data, the behavior of χ^2_{dof}, as displayed in Figs. 29–31, resolve precise optimal regularization scales: $\Lambda^{c_0}_{\mathrm{central}} = 0.72$ GeV, $\Lambda^{c_2}_{\mathrm{central}} = 0.71$ GeV and $\Lambda^{c_4}_{\mathrm{central}} = 0.71$ GeV. The systematic errors obtained from each χ^2_{dof} curve seem arbitrarily constrained as a consequence of including more data points, which extend well outside the chiral regime, and possibly outside the applicable region of FRR techniques. This issue is addressed in the ensuing section.

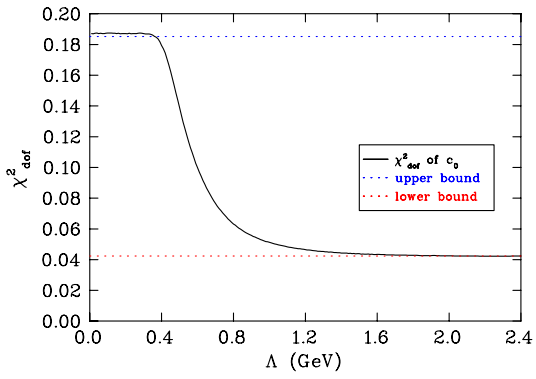

FIG. 26 (color online). χ^2_{dof}, for c_0 versus Λ, corresponding to the renormalization flow curves displayed in Fig. 23. A lower bound for the regularization scale is found: $\Lambda^{c_0}_{\mathrm{lower}} = 0.39$ GeV.

C. Optimal pion mass region

In this section, a robust method for determining an optimal range of pion masses is presented. This range corresponds to an optimal number of simulation results to be used for fitting. First, consider the extrapolation of the quenched ρ meson mass, which can now be completed. The statistical uncertainties in the values of c_0, c_2, c_4 are dependent on $m^2_{\pi,\mathrm{max}}$. As a consequence, the uncertainty in the extrapolated ρ meson mass m^{ext}_{ρ} must also be dependent on $m^2_{\pi,\mathrm{max}}$. Since the estimate of the statistical uncertainty in an extrapolated point will tend to decrease as more

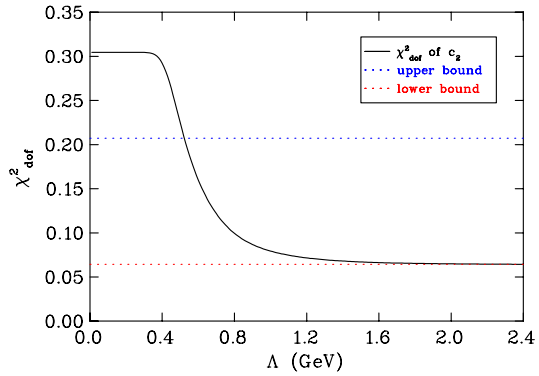

FIG. 27 (color online). χ^2_{dof}, for c_2 versus Λ, corresponding to the renormalization flow curves displayed in Fig. 24. A lower bound for the regularization scale is found: $\Lambda^{c_2}_{\mathrm{lower}} = 0.52$ GeV.

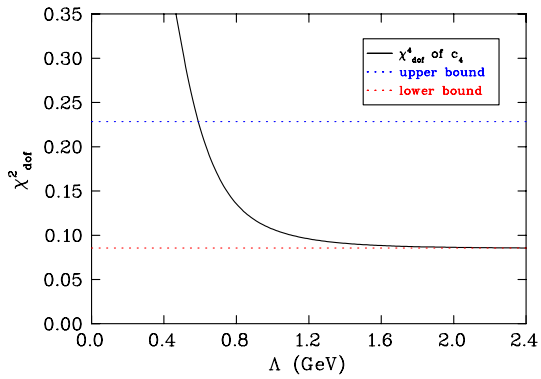

FIG. 28 (color online). χ^2_{dof}, for c_4 versus Λ, corresponding to the renormalization flow curves displayed in Fig. 25. A lower bound for the regularization scale is found: $\Lambda^{c_4}_{\mathrm{lower}} = 0.59$ GeV.

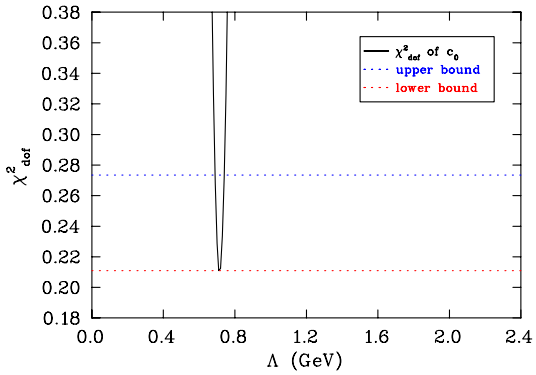

FIG. 29 (color online). $\chi^2_{\rm dof}$, for c_0 versus Λ, corresponding to all available data, including the low-energy set.

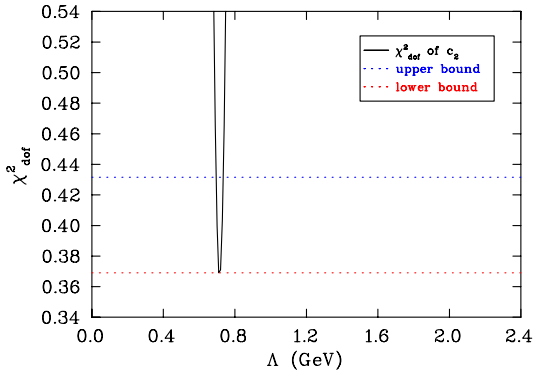

FIG. 30 (color online). $\chi^2_{\rm dof}$, for c_2 versus Λ, corresponding to all available data, including the low-energy set.

data are included in the fit, one might naïvely choose to use the largest $m^2_{\pi,\rm max}$ value possible in the data set. However, at some large value of $m^2_{\pi,\rm max}$, FRR χEFT will not provide a valid model for obtaining a suitable fit. At this upper bound of applicability for FRR χEFT, the uncertainty in an extrapolated point is dominated by the systematic error in the underlying parameters. This is due to a greater scheme dependence in extrapolations using data extending outside

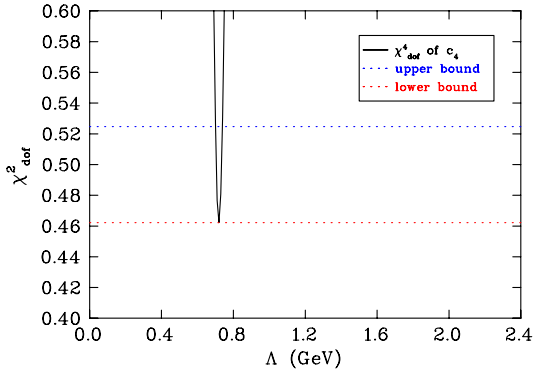

FIG. 31 (color online). $\chi^2_{\rm dof}$, for c_4 versus Λ, corresponding to all available data, including the low-energy set.

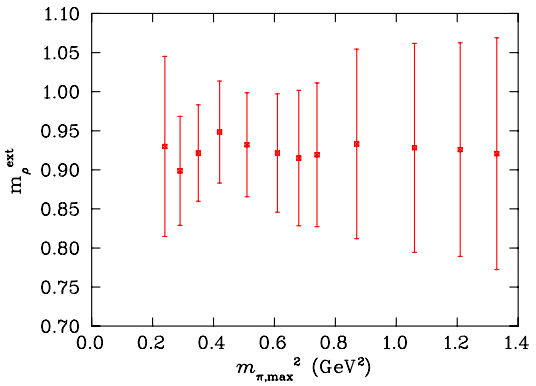

FIG. 32 (color online). behavior of the extrapolation of the quenched ρ meson mass to the physical point $m^{\rm ext}_{\rho,Q}(m^2_{\pi,\rm phys})$ vs $m^2_{\pi,\rm max}$ using the initial data set, which excludes the lowest mass data points. In each case, c_0 is obtained using the scale $\Lambda_{\rm central}$ (for a triple-dipole regulator) as obtained from the $\chi^2_{\rm dof}$ analysis. The error bars include the statistical and systematic uncertainties in c_0 added in quadrature. The optimal value $\hat{m}^2_{\pi,\rm max} = 0.35\ {\rm GeV}^2$.

the PCR, meaning that the extrapolations are more sensitive to changes in the parameters of the loop integrals. Thus there is a balance point $m^2_{\pi,\rm max} = \hat{m}^2_{\pi,\rm max}$, where the statistical and systematic uncertainties (added in quadrature) in an extrapolation are minimized.

In order to obtain this value $\hat{m}^2_{\pi,\rm max}$, consider the behavior of the extrapolation of the ρ meson mass to the physical point $m^{\rm ext}_{\rho,Q}(m^2_{\pi,\rm phys})$, as a function of $m^2_{\pi,\rm max}$. Treating the parameters: $\Lambda^{\rm scale}$, g_2, g_4, M_0^2 and A_0 as independent, their systematic uncertainties from these sources are added in quadrature. In addition, the systematic uncertainty due to the choice of the regulator functional form is roughly

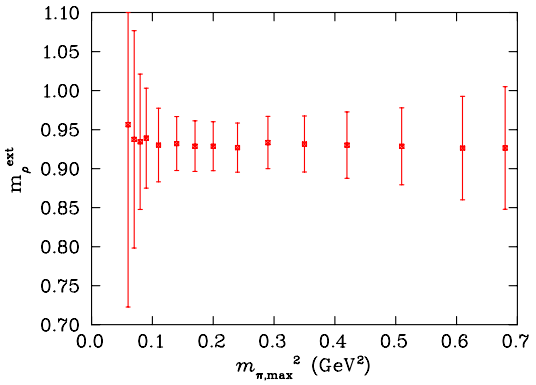

FIG. 33 (color online). behavior of the extrapolation of the quenched ρ meson mass to the physical point $m^{\rm ext}_{\rho,Q}(m^2_{\pi,\rm phys})$ vs $m^2_{\pi,\rm max}$ using the complete data set, which includes the lowest mass data points. In each case, c_0 is obtained using the scale $\Lambda_{\rm central}$ (for a triple-dipole regulator) as obtained from the $\chi^2_{\rm dof}$ analysis. The error bars include the statistical and systematic uncertainties in c_0 added in quadrature. The optimal value $\hat{m}^2_{\pi,\rm max} = 0.20\ {\rm GeV}^2$.

TABLE III. Results for the quenched ρ meson mass for different values of $m^2_{\pi,\max}$, extrapolated to the physical point, corresponding to Figs. 32 (for the original data set) and 33 (for the complete data set). The uncertainty in $m^{\text{ext}}_{\rho,Q}(m^2_{\pi,\text{phys}})$ is provided in the following order: the statistical uncertainty, the systematic uncertainty due to the intrinsic scale, g_2, g_4, M_0^2, A_0 and the regulator functional form, respectively.

$m^2_{\pi,\max}$ (GeV^2)	$m^{\text{ext}}_{\rho,Q}(m^2_{\pi,\text{phys}})$ (GeV): original set	$m^{\text{ext}}_{\rho,Q}(m^2_{\pi,\text{phys}})$ (GeV): complete set
0.059	⋯	0.956(234)(1)(0)(0)(1)(0)(0)
0.068	⋯	0.938(139)(1)(1)(0)(1)(0)(0)
0.080	⋯	0.934(87)(1)(1)(0)(1)(0)(0)
0.094	⋯	0.939(64)(2)(1)(0)(1)(0)(1)
0.114	⋯	0.930(47)(3)(2)(0)(2)(0)(0)
0.143	⋯	0.932(34)(5)(3)(0)(4)(1)(0)
0.172	⋯	0.929(31)(6)(4)(0)(5)(1)(0)
0.204	⋯	0.929(29)(9)(5)(0)(6)(1)(0)
0.241	0.930(110)(27)(14)(0)(17)(4)(6)	0.927(27)(12)(7)(0)(9)(2)(0)
0.288	0.899(62)(31)(1)(0)(1)(1)	0.933(24)(17)(10)(0)(12)(3)(1)
0.347	0.922(43)(37)(11)(0)(13)(28)(17)	0.932(23)(21)(11)(0)(13)(3)(4)
0.422	0.948(29)(45)(23)(1)(28)(7)(8)	0.930(20)(29)(14)(0)(16)(4)(8)
0.515	0.932(23)(51)(19)(1)(23)(6)(19)	0.929(19)(37)(15)(0)(18)(4)(13)
0.610	0.921(18)(63)(18)(1)(22)(5)(25)	0.926(16)(54)(18)(0)(21)(5)(22)
0.676	0.915(12)(74)(18)(1)(22)(6)(32)	0.926(14)(66)(19)(1)(23)(6)(25)
0.743	0.919(13)(79)(22)(1)(26)(7)(29)	0.922(12)(74)(21)(1)(26)(7)(27)
0.867	0.933(9)(103)(32)(1)(39)(12)(35)	0.923(8)(100)(29)(1)(35)(11)(38)
1.062	0.928(7)(115)(32)(1)(38)(12)(43)	⋯
1.212	0.926(7)(121)(31)(1)(37)(12)(38)	⋯
1.329	0.921(6)(132)(31)(1)(37)(12)(43)	⋯
1.742	0.915(5)(146)(30)(1)(37)(13)(48)	⋯
2.187	0.910(4)(175)(30)(1)(37)(14)(55)	⋯
3.150	0.902(3)(197)(29)(1)(36)(14)(61)	⋯

estimated by comparing the results using the double-dipole and the step function. These functional forms are the two most different forms of the various regulators considered, since the dipole was excluded due to the extra nonanalytic contributions it introduces. The results for the initial and complete data sets are shown in Figs. 32 and 33, respectively. Note that the systematic uncertainty due to Λ^{scale} is included for chiral order $\mathcal{O}(m_\pi^4)$.

Figure 32 indicates an optimal value $\hat{m}^2_{\pi,\max} = 0.35$ GeV^2, which will be used in the final extrapolations, in order to check the results of this method with the low-energy data. By using only the data contained in the optimal pion mass region, constrained by $\hat{m}^2_{\pi,\max}$, an estimate of the optimal regularization scale may be calculated with a more generous corresponding systematic uncertainty. The value $\Lambda^{\text{scale}} = 0.64$ GeV is the average of $\Lambda^{\text{scale}}_{c_0}$, $\Lambda^{\text{scale}}_{c_2}$ and $\Lambda^{\text{scale}}_{c_4}$ using this method. The χ^2_{dof} analysis does not provide an upper or lower bound at this value of $\hat{m}^2_{\pi,\max}$. Note that these two estimates of the optimal regularization scale are consistent with each other. Both shall be used and compared in the final analysis. Figure 33 indicates an optimal value $\hat{m}^2_{\pi,\max} = 0.20$ GeV^2 for the

TABLE IV. The values of c_0, c_2 and c_4 as obtained from both the original data set and the complete set, which includes the low-energy data. In each case, the coefficients are evaluated using the scale Λ_{central} (for a triple-dipole regulator) as obtained from the χ^2_{dof} analysis. The value of $m^2_{\pi,\max}$ used is that which yields the smallest error bar in adding statistical and systematic uncertainties in quadrature. For the initial data set, $\hat{m}^2_{\pi,\max} = 0.35$ GeV^2. For the complete data set, $\hat{m}^2_{\pi,\max} = 0.20$ GeV^2. The statistical uncertainty is quoted in the first pair of parentheses, and the systematic uncertainty is quoted due to the parameters, in the following order: Λ^{scale}, g_2, g_4, M_0^2, A_0 and the regulator functional form.

	c_0 (GeV^2)	c_2	c_4 (GeV^{-2})
original set	1.31(5)(10)(4)(0)(5)(4)(8)	7.9(4)(25)(2)(0)(2)(1)(4)	−16.2(7)(382)(3)(0)(3)(1)(4)
complete set	1.35(4)(3)(36)(16)(60)(166)(113)	6.8(5)(17)(13)(1)(17)(14)(11)	−3.3(16)(359)(23)(1)(28)(12)(1)

complete data set, which includes the low-energy data. A higher density of data in the low-energy region serves to decrease the statistical error estimate of extrapolations to the low-energy region. The corresponding value of Λ^{scale} is unconstrained in this case, since the data lie close to the PCR. The breakdown of the systematic error bar into its constituent uncertainties is listed in Table III.

The values of c_0, c_2 and c_4 for both the original data set and the complete data set are shown in Table IV, with statistical error estimate quoted first and systematic uncertainty due to the parameters Λ^{scale}, g_2, g_4, M_0^2, A_0, and the regulator functional form quoted second, in this order. In the case of the original data set, the value of c_4 is not well-determined, due to the small number of data points used. In the case of the complete data set, the results are dominated by statistical uncertainty and also result in an almost unconstrained value of c_4. Even if Λ^{scale} is quite well-determined, as observed in Figs. 17–19, the value of c_4 itself is sensitive to changes in the regularization scale Λ, as evident from Fig. 16. The coefficients of the complete set are less well-determined due to the fact that $\hat{m}^2_{\pi,\text{max}} = 0.20\ \text{GeV}^2$, leaving only low-energy results with large statistical uncertainties for fitting.

The result using the estimate of the optimal regularization scale $\Lambda^{\text{scale}} = 0.64$ GeV, with the systematic uncertainty calculated by varying Λ across all suitable values, and using the initial data set, is shown in Fig. 34. The extrapolation to the physical point obtained for this quenched data set is $m^{\text{ext}}_{\rho,Q}(m^2_{\pi,\text{phys}}) = 0.922^{+0.065}_{-0.060}$ GeV, an uncertainty of approximately 7%. Figure 35 shows the data plotted with error bars correlated relative to the lightest data point in the original set, $m^2_\pi = 0.143\ \text{GeV}^2$, using $\Lambda_{\text{scale}} = 0.64$ GeV, and varying Λ across its full range of values. This naturally increases the estimate of the systematic uncertainty of the extrapolations, but also serves to demonstrate how closely the results from lattice QCD and χEFT match.

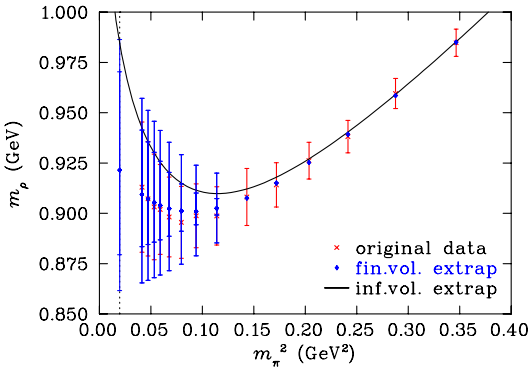

FIG. 34 (color online). Comparison of chiral extrapolation predictions (blue diamond) with Kentucky Group data (red cross). Extrapolation is performed at $\Lambda_{\text{scale}} = 0.64$ GeV, varied across the whole range of Λ values, and using the optimal number of data points, corresponding to $\hat{m}^2_{\pi,\text{max}} = 0.35\ \text{GeV}^2$. The inner error bar on the extrapolation points represents purely the systematic error from parameters. The outer error bar represents the systematic and statistical error estimates added in quadrature.

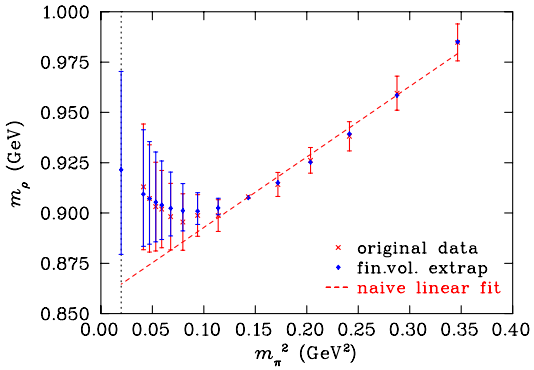

FIG. 35 (color online). Comparison of chiral extrapolation predictions (blue diamond) with Kentucky Group data (red cross), with errors correlated relative to the point at $m^2_\pi = 0.143\ \text{GeV}^2$. This is done simply to clarify the plot in Fig. 34 by removing much of the correlated statistical error. Extrapolation is performed at $\Lambda_{\text{scale}} = 0.64$ GeV, varied across the whole range of Λ values, and using the optimal number of data points, corresponding to $\hat{m}^2_{\pi,\text{max}} = 0.35\ \text{GeV}^2$. The error bar on the extrapolation points represents the systematic error only. A simple linear fit, on the optimal pion mass region, is included for comparison.

V. CONCLUSION

A technique for isolating an optimal regularization scale, established in Ref. [4], was tested in quenched QCD through an examination of the quenched ρ meson mass. The result is a successful extrapolation based on an extended effective field theory procedure. By using quenched lattice QCD results that extended beyond the power-counting regime, an optimal regularization scale was obtained from the renormalization flow of the low-energy coefficients.

An optimal value of the maximum pion mass to be used for fitting was also calculated, and this resulted in an alternative estimate of the value of the optimal regularization scale, which was consistent with the first result. The mass of the ρ meson was calculated in the low-energy region, including the physical point, using each estimate of the optimal regularization scale, and both results were compared. The results of extrapolations using χEFT, and the results of lattice QCD simulations, were demonstrated to be consistent. The extrapolation correctly predicts the low-energy curvature that was observed when the low-energy lattice simulation results were revealed.

In full QCD, using dynamical fermions, the process $\rho \to \pi\pi$ contributes to the ρ meson mass. This means that near the chiral limit, the $\pi\pi$ component of the ρ necessarily involves a hard momentum scale, and therefore is not

amenable to the standard methods of low-energy expansions, as entailed by χPT. Therefore, one needs to resort to alternative techniques in such instances.

However, since there exists no experimental value for the mass of a particle in the quenched approximation, this analysis demonstrates the ability of the technique to make predictions without phenomenologically motivated bias. The results clearly indicate a successful procedure for using lattice QCD data outside the power-counting regime to extrapolate an observable to the chiral regime.

ACKNOWLEDGMENTS

We would like the thank Professor T. Cohen for helpful discussions. This research is supported by the Australian Research Council through Grant No. DP110101265. Thanks go to U.S. DOE Grant No. DE-FG05-84ER40154 for partial support. The research of N. Mathur is supported under Grant No. DST-SR/S2/RJN-19/2007, India. The research of J. B. Zhang is supported by Chinese NSFC Grant No. 10835002 and Science Foundation of Chinese University.

[1] S. Aoki *et al.* (PACS-CS Collaboration), Phys. Rev. D **79**, 034503 (2009).
[2] Y. Kuramashi, Proc. Sci., LATTICE2008 (2008) 018 [arXiv:0811.2630].
[3] S. Durr, Z. Fodor, C. Hoelbling, S. Katz, and S. Krieg *et al.*, J. High Energy Phys. 08 (2011) 148.
[4] J. M. M. Hall, D. B. Leinweber, and R. D. Young, Phys. Rev. D **82**, 034010 (2010).
[5] R. D. Young, J. M. M. Hall, and D. B. Leinweber, arXiv:0907.0408.
[6] C.-K. Chow and S.-J. Rey, Nucl. Phys. **B528**, 303 (1998).
[7] W. Armour, C. R. Allton, D. B. Leinweber, A. W. Thomas, and R. D. Young, J. Phys. G **32**, 971 (2006).
[8] M. Gell-Mann, R. J. Oakes, and B. Renner, Phys. Rev. **175**, 2195 (1968).
[9] R. D. Young, D. B. Leinweber, and A. W. Thomas, Prog. Part. Nucl. Phys. **50**, 399 (2003).
[10] D. B. Leinweber, A. W. Thomas, and R. D. Young, Nucl. Phys. **A755**, 59 (2005).
[11] M. Booth, G. Chiladze, and A. F. Falk, Phys. Rev. D **55**, 3092 (1997).
[12] S. R. Sharpe, Nucl. Phys. B, Proc. Suppl. **53**, 181 (1997).
[13] M. Lublinsky, Phys. Rev. D **55**, 249 (1997).
[14] A. Duncan, E. Eichten, S. Perrucci, and H. Thacker, Nucl. Phys. B, Proc. Suppl. **53**, 256 (1997).
[15] Y. Iwasaki, Nucl. Phys. **B258**, 141 (1985).
[16] H. Neuberger, Phys. Rev. D **57**, 5417 (1998).
[17] S. J. Dong *et al.*, Phys. Rev. D **65**, 054507 (2002).
[18] Y. Chen *et al.*, Phys. Rev. D **70**, 034502 (2004).
[19] J. B. Zhang *et al.*, Phys. Rev. D **72**, 114509 (2005).
[20] H. Leutwyler and A. V. Smilga, Phys. Rev. D **46**, 5607 (1992).
[21] A. Li *et al.* (xQCD Collaboration), Phys. Rev. D **82**, 114501 (2010).